

II. A PHYSICAL OPTICS/ EQUIVALENT CURRENTS MODEL FOR THE RCS OF TRIHEDRAL CORNER REFLECTORS

A. INTRODUCTION

In the last report we examined the radar cross section (RCS) of the square trihedral corner reflector in the interior region. Expressions for the reflected fields as well as expressions for the equivalent currents at the edges of the trihedral were explicitly given. In this report we examine the RCS of both the square and triangular corner reflectors. The formulation of the reflected fields for the interior region of the triangular trihedral is exactly the same as that of the square trihedral; however, the area over which the Physical Optics (PO) surface integral is evaluated is now different. The approach followed to determine this area of integration is explained thoroughly in this report. The equivalent currents at the exterior edges of either trihedral were derived based upon Michaeli's PTD equivalent edge currents. The PTD-EEC expressions for the triangular trihedral are also similar to those already used in the case of the square trihedral but now the orientation of the edges is different. Furthermore, in this report we include more results, for both the square and triangular trihedrals, which are compared with Finite-Difference Time-Domain (FDTD) data as well as with measurements performed in the ElectroMagnetic Anechoic Chamber (EMAC) at Arizona State University. The PO-MEC results compare very well with both the FDTD data and the measured data.

Analysis of a square trihedral corner reflector was performed by Baldauf *et al.* [22], using the CAD-based Shooting and Bouncing Ray (SBR) method. They examined both its monostatic and bistatic RCS for three different sizes (small, medium, and large). Their results were good for medium and large trihedrals but less accurate for smaller objects. The SBR method has the disadvantage that both

its accuracy and the CPU time required to run a particular case depend on the number of rays per wavelength launched from the incident direction toward the target. Increasing the density of the rays leads to more accurate results but at the expense of extending the CPU time. The accuracy of the method is proportional to the number of rays because the fields at the aperture of the output ray tube are approximated to those that correspond to the ray passing through the center of the aperture. As the number of rays per wavelength increases, the area of the aperture eventually becomes very small and the approximation becomes more appropriate. In other words, the smaller the aperture of the output ray tube is, the more accurate the SBR results are; however, the CPU time increases because of the use of a denser grid. Also, the CPU time increases with increasing radar target size. This is not a very attractive feature for a high frequency approach such as the SBR method.

In the present analysis, PO and Michaeli's equivalent edge currents (EEC) method (usually referred as PTD-EEC) are applied on both the square and triangular trihedral corner reflectors to evaluate the backscatter RCS in the interior region. PO is used for the calculation of single, double, and triple reflections from the trihedral plates, whereas PTD-EEC is used for the calculation of the first-order diffractions from the exterior edges. The PO surface current density is integrated over the illuminated area of the particular plate. For single reflections the surface integration is evaluated over the entire plate because it is completely illuminated. The integration is carried out in closed form since the integrand is a simple exponential function with linearly varying phase over the entire surface of the plate. For double and triple reflections, however, the surface of integration is not the entire area of the second and third plates, respectively, but rather only the illuminated parts of these plates. The shape of the illuminated area is usually an arbitrary polygon whose shape changes according to the incident and observation angles. The difficulty in this case is to determine the shape of the illuminated area at any incident angle and to efficiently integrate the surface current density over

that area. Another problem with the evaluation of the double and triple reflected fields is the fact that the surface current density on the second and third plates of the trihedral should be calculated in the “near field” of the first and second reflections, respectively. In our analysis, however, the GO approximation is used for the calculation of the initial reflected fields and the PO is subsequently applied only for the last reflection. In other words, it is assumed that the planar nature of the incident wave is maintained after the first and second reflections, which simplifies the expressions for the scattered fields considerably.

For the evaluation of the diffracted fields, Michaeli's PTD-EEC expressions are utilized to calculate the first-order diffractions from the exterior edges of the trihedral. Diffractions from interior edges are usually much lower than diffractions from exterior edges and, therefore, were excluded. PTD-EEC expressions are based on the fringe component of the equivalent edge current for the wedge. These were deduced from the exact solution of the canonical wedge problem. It is also important to note that PTD-EEC expressions do not contain the PO component of equivalent currents; therefore, the diffracted fields using PTD-EEC should improve the reflected fields calculated using PO. In the case of the trihedral, however, the reflected fields in the interior region are significantly higher than the diffracted fields. Consequently, the effect of the diffractions is not always obvious.

B. ANALYSIS

The backscatter cross section of the square and triangular trihedral corner reflectors, depicted in Figs. 17(a) and 17(b), is evaluated by considering single, double, and triple reflections as well as first-order diffractions. Expressions for the reflected fields were given explicitly in the previous report; therefore, they are not repeated here. It is important, however, that the approach used to determine the shape of the illuminated area on the plate of last reflection be explained in detail. This is the area on which the PO integration is evaluated. For single reflections the illuminated area is the entire surface of the particular plate. For double and

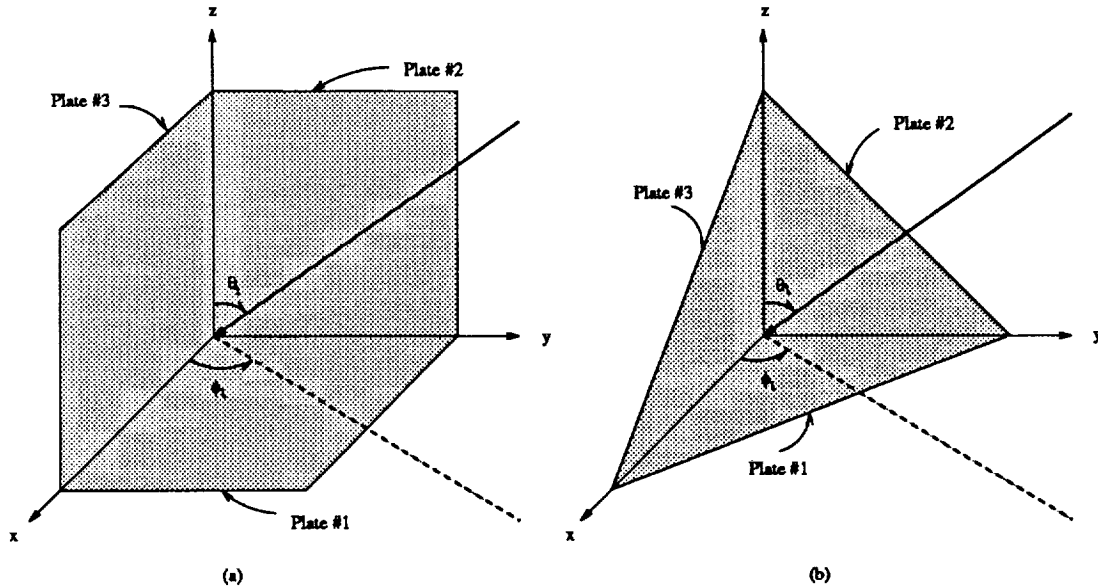


Figure 17: Geometry of the square and triangular trihedrals.

triple reflections the illuminated area looks like an arbitrary polygon whose shape depends on the incident angles.

1. The Shape of the Illuminated Area for Double and Triple Reflections

Evaluation of the doubly and triply reflected fields requires integration over the illuminated part of the plate on which the last reflection occurs. The illuminated area on that plate has the shape of a polygon whose corner coordinates vary according to the direction of incidence. Our objective in this section is to explain how the corner coordinates of the illuminated area can be determined, as well as to illustrate an efficient way to evaluate the PO surface integral over this area.

Double and triple reflections occurring in the interior of a trihedral corner reflector create shadow regions on the second and third plate, respectively. Fig. 18(a) illustrates the shaded area created on plate #3 for the case of the double reflection term R_{23} . As is shown, the incident plane wave, which illuminates completely all three trihedral plates, is first reflected from plate #2 and then propagates toward plate #3. However, the reflected fields from plate #2 do not completely illuminate plate #3. To determine the shape of the illuminated and/or shadow region

on plate #3, it is first necessary to obtain the direction of the rays after the first reflection occurs. Their direction, according to image theory, is the mirror image of the incident direction over plate #2. Knowing the direction of the reflected rays from plate #2, one can trace the path of the rays that pass through the exterior edges of plate #2, as shown in Fig. 18(a), to the point where they reach the surface of plate #3. We do not trace the path of the rays that do not strike plate #3. The line connecting the points where these ray-paths intersect with plate #3, referring to Fig. 18(a), defines the boundary that separates the illuminated from the shadow region. The illuminated area should always include the origin of the coordinate system. Note that the shape of the illuminated area varies with the incident angle. To illustrate this, two cases with different directions of incidence are examined. Fig. 18(a) depicts the shadow region on plate #3 for incident angles θ_i greater than 45° and ϕ_i also greater than 45° . As θ_i becomes smaller than 45° , the shape of the illuminated area looks like a triangle, as shown in Fig. 18(b).

For triple reflections, estimating the shaded part on the third plate after two consecutive reflections on the other two trihedral plates is much more complicated than in the case of double reflections. The approach, however, remains the same as before — the double reflected rays passing through the periphery of the illuminated area on the second plate, see Fig. 18(c), are traced to the third plate. These rays intersect the surface of the third plate at certain points, which actually mark the boundary of the illuminated area (or shaded area). The shaded area on the third plate for the case of the triple reflection term R_{123} is illustrated in Fig. 18(c).

As demonstrated above, the illuminated area on a particular plate due to either double or triple reflection is a polygon whose shape depends on the direction of wave incidence. To calculate the reflected fields, the PO surface integral should be evaluated on this polygon. An efficient way to evaluate this integral is to subdivide the corresponding polygon into rectangles and right triangles. The PO surface integral can then be easily evaluated over the areas of both these two shapes in closed form.

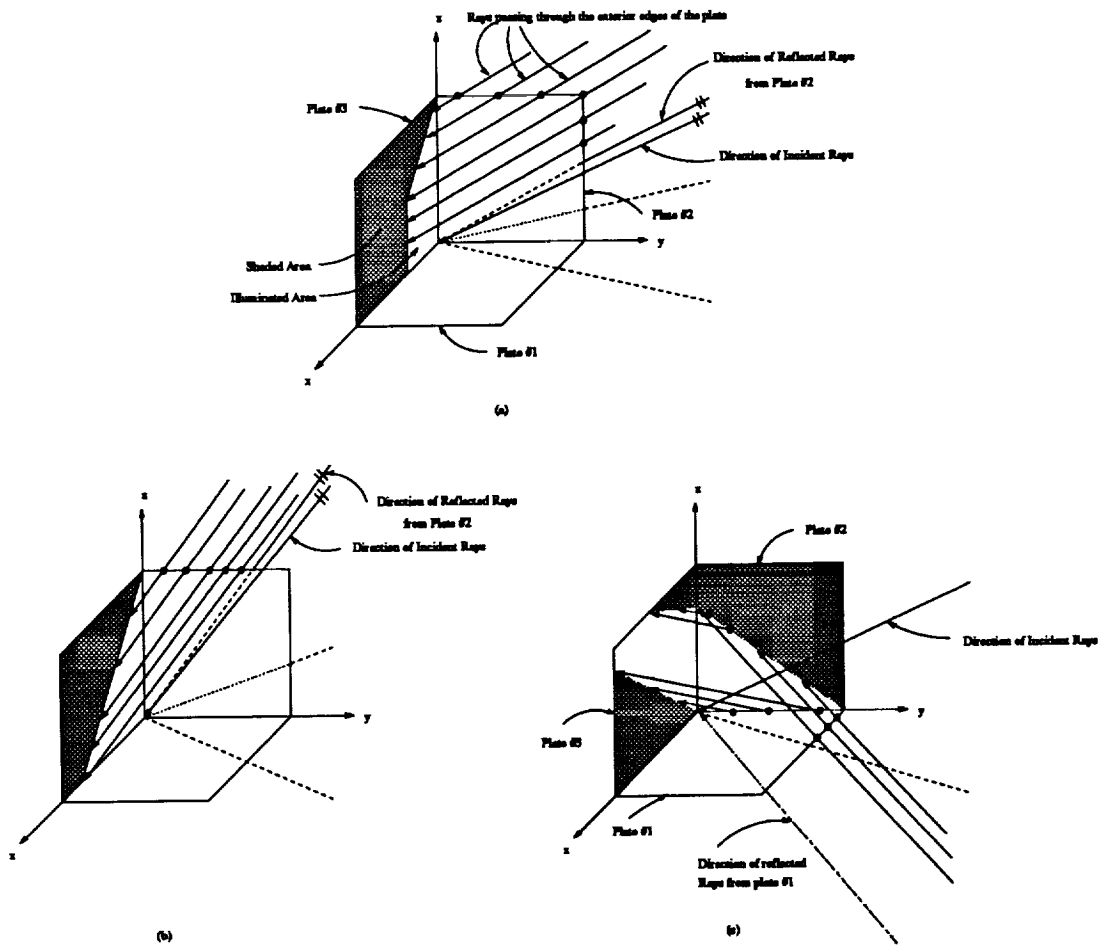


Figure 18: Shading due to multiple reflections by the interior of the trihedral.

2. Evaluation of Diffracted Fields Using PTD-EEC

PTD-EEC expressions, derived by Michaeli [23, 24], are utilized to find the far-field diffracted fields from the exterior edges of both the square and the triangular trihedral corner reflectors. PTD-EEC expressions are based on the fringe currents that exist at the edges. Unlike GTD-EEC, PTD-EEC does not include the PO surface current density. Therefore, adding the diffracted fields (based on the PTD-EEC formulations) to the reflected fields (based on the PO surface current density) results in closer agreement with the experimental data. The corresponding expressions for the fringe currents, I^f and M^f , can be found in Michaeli's papers on equivalent currents [23, 24]. Here, the analysis is restricted to how the electric and magnetic fringe currents are used to derive expressions for the far-field diffracted fields. The procedure is similar to the one used for the reflected fields in the previous section. First, the vector potentials are estimated using

$$\mathbf{A} = \frac{\mu}{4\pi} \int_C \mathbf{I}^f \frac{e^{-jkR}}{R} dl \simeq \frac{\mu}{4\pi} \frac{e^{-jk r}}{r} \int_C \mathbf{I}^f e^{jkL_s} dl \quad (6)$$

$$\mathbf{F} = \frac{\epsilon}{4\pi} \int_C \mathbf{M}^f \frac{e^{-jkR}}{R} dl \simeq \frac{\epsilon}{4\pi} \frac{e^{-jk r}}{r} \int_C \mathbf{M}^f e^{jkL_s} dl \quad (7)$$

where L_s was defined in the previous report. The integral is evaluated along the length of the trihedral edge from which the diffracted fields are to be calculated. As in the case of reflected fields from a trihedral plate, this integral can be evaluated in closed form because the integrand is a simple exponential function with linearly varying phase along the edge. After evaluating the electric and magnetic vector potentials, the far-field spherical components of the scattered field can be written as [25]

$$E_r \simeq 0 \quad (8)$$

$$E_\theta \simeq -j\omega(A_\theta + \eta F_\phi) \quad (9)$$

$$E_\phi \simeq -j\omega(A_\phi - \eta F_\theta) \quad (10)$$

C. RESULTS

Results from the combined PO-MEC model are compared with experimental data, as well as with data obtained using the FDTD method. The experiments were performed using both a square and a triangular corner reflector whose geometries are shown in Figs. 17(a) and 17(b).

The main advantage of the PO-MEC approach, over other techniques, is that it calculates each scattering component separately and then combines them for the calculation of the total RCS. Each component (single, double, triple reflections and first-order diffractions), therefore, can be plotted separately in order to examine its contribution to the total RCS. Then, the shape of the particular target can be slightly modified to reduce the RCS of the component that contributes the most to the total backscattered fields. Fig. 19 illustrates the major individual backscattering components of a 15λ square trihedral for $\theta_i = \theta_s = 50^\circ$ and $\phi_i = \phi_s$, varying from 0° to 90° . These RCS plots represent single reflections (R_1 , R_2 , and R_3), double reflections (R_{12} , R_{13} , R_{21} , R_{23} , R_{31} , and R_{32}), triple reflections (R_{123} , R_{132} , R_{213} , R_{231} , R_{312} , and R_{321}), and first-order diffractions from the exterior edges of the square trihedral plates. Diffractions from the three interior edges of the trihedral were not considered, which explains why the RCS pattern for the first-order diffractions is not completely symmetric about 45° . Fig. 19 also illustrates the total RCS pattern of the square trihedral. Examining these five figures, it can be seen that the major contribution to the RCS is provided by the triply reflected fields. The reason is that all three trihedral plates are mutually perpendicular; therefore, the direction of propagation of the triply reflected fields is parallel to that of the incident plane wave. Changing the angle between the plates will certainly reduce the overall RCS.

To adequately validate the approach followed in this paper, different sizes of both trihedral corner reflectors were considered. All graphs in this section correspond to E_θ polarization.

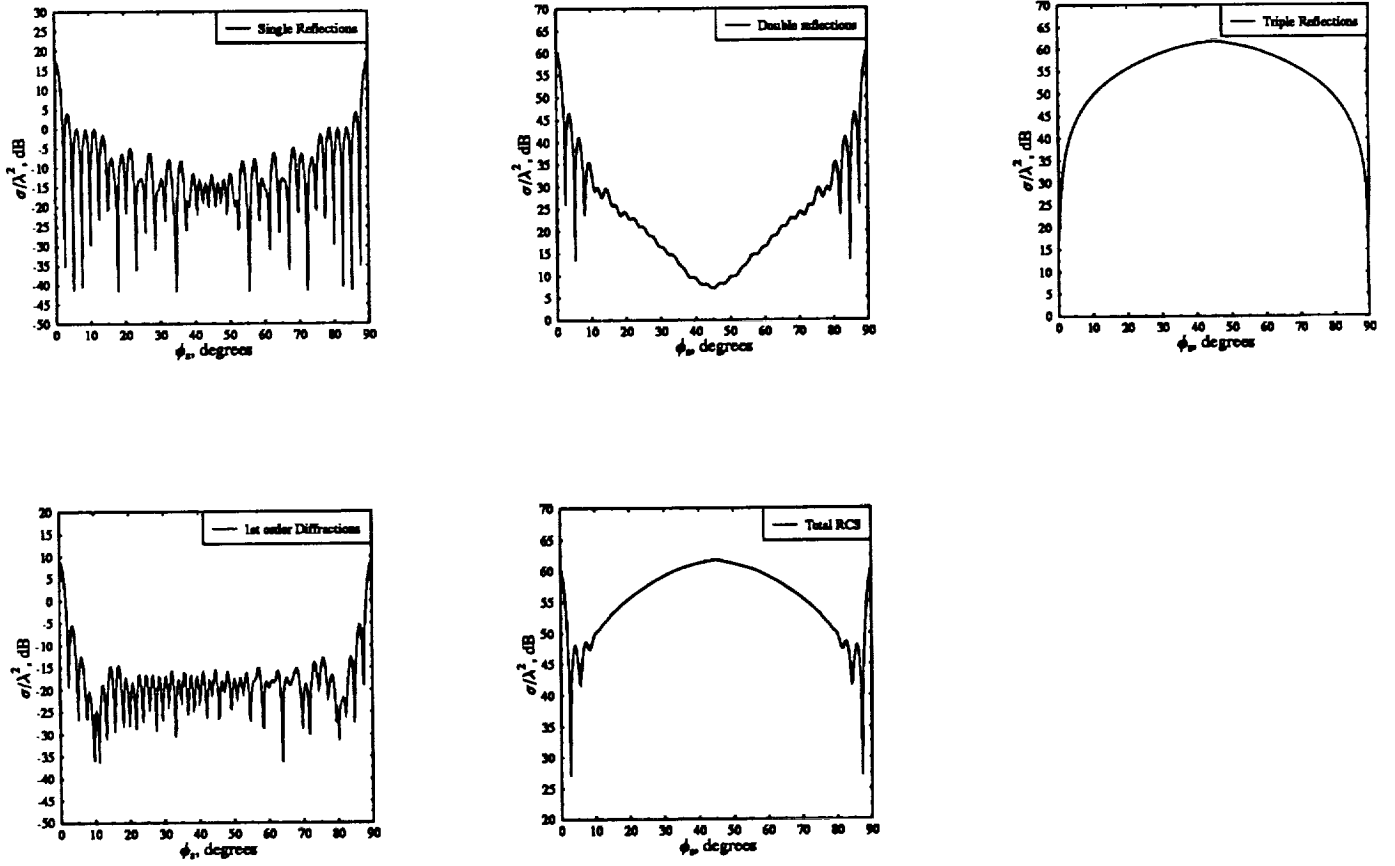


Figure 19: Breakdown of scattering into individual components.

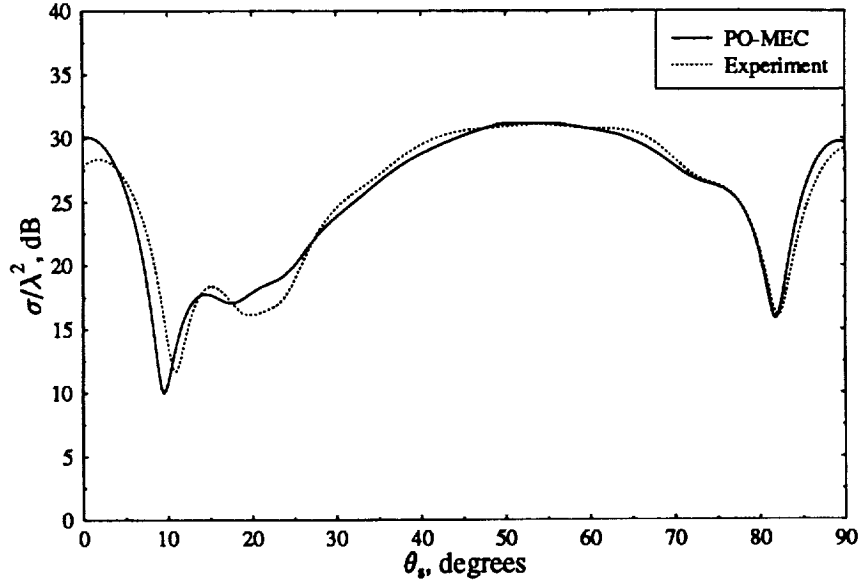


Figure 20: Monostatic RCS of a 3λ square trihedral at $\phi_i = \phi_s = 60^\circ$.

1. Small Trihedral Corner Reflectors

A 3λ square trihedral and a 5λ triangular trihedral are considered relatively small radar targets for high frequency analysis. The classification of small, medium and large trihedrals is based on the total area covered by the trihedral plates. Fig. 20 shows the monostatic RCS of a 3λ square trihedral at $\phi_i = \phi_s = 60^\circ$ as $\theta_i = \theta_s$ varies from 0° to 90° . The agreement between the predicted and the experimental results is good even if the object is relatively small for high frequency analysis. Fig. 21 shows the monostatic RCS of a 5λ triangular trihedral at $\phi_i = \phi_s = 35^\circ$ as $\theta_i = \theta_s$ varies from 0° to 90° . A very good agreement between the theoretical and the experimental results is observed.

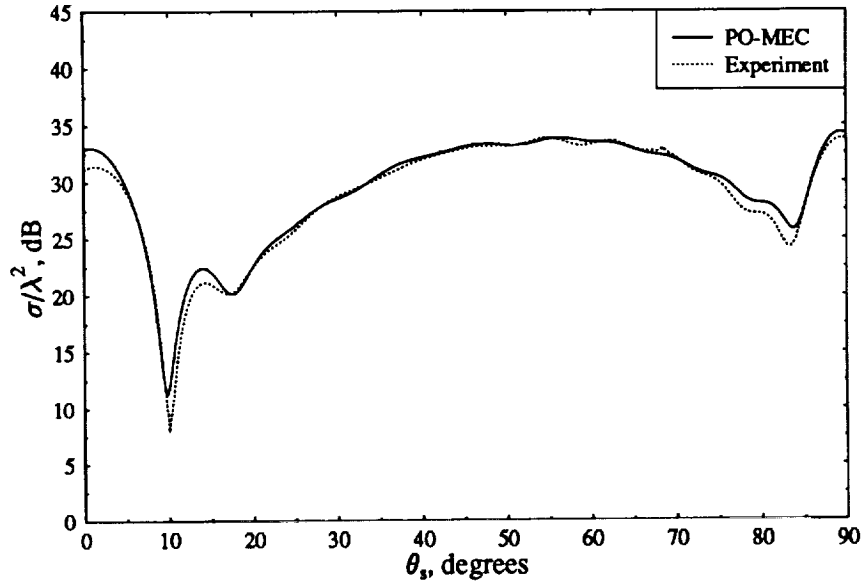


Figure 21: Monostatic RCS of a 5λ triangular trihedral at $\phi_i = \phi_s = 35^\circ$.

2. Medium Trihedral Corner Reflectors

A 5λ square trihedral and a 7λ triangular trihedral are considered medium sized radar targets. Fig. 22 shows the monostatic RCS of the 5λ square trihedral on a conical path where $\theta_i = \theta_s = 66^\circ$ and $\phi_i = \phi_s$ varies from 0° to 90° . Our predictions are compared with both FDTD and measured data. The agreement is very good.

In addition to conical paths, our formulation is capable of calculating the RCS of either the square or triangular trihedral by moving the source and/or observation point along a great circle. The great circle has its center at the origin of the coordinate system and makes an angle $\theta = \theta_g$ with the z-axis at $\phi = 45^\circ$. This is the same as if the trihedral is tilted forward so its z-directed edge makes an angle $90 - \theta_g$ degrees with the z-axis as ϕ_s changes from 0° to 90° . Fig. 23 shows the monostatic RCS of a 7λ triangular trihedral as ϕ_s varies on a great circle at $\theta_g = 80^\circ$. The agreement between theoretical and experimental data is very good. Also, observe that the RCS patterns of Figs. 22 and 23 are symmetric about

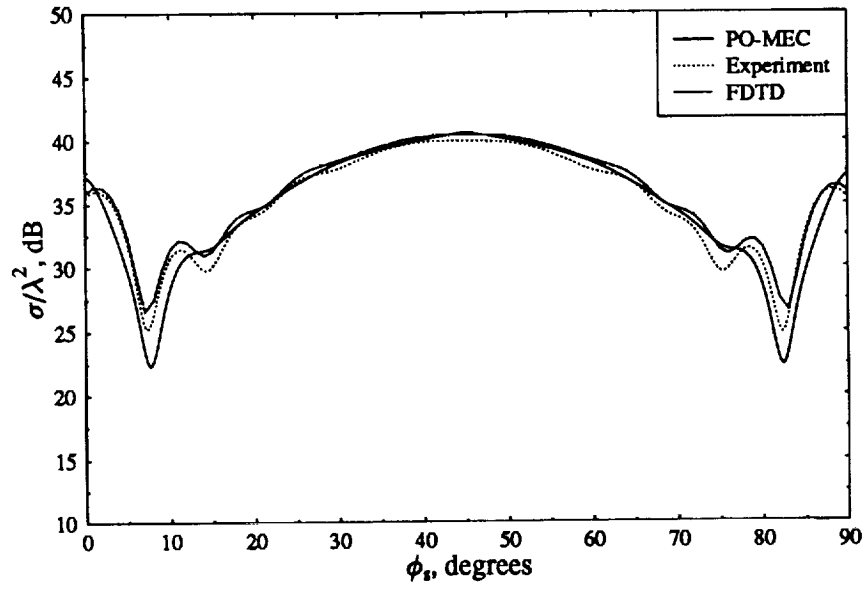


Figure 22: Monostatic RCS of a 5λ square trihedral at $\theta_i = \theta_s = 66^\circ$.

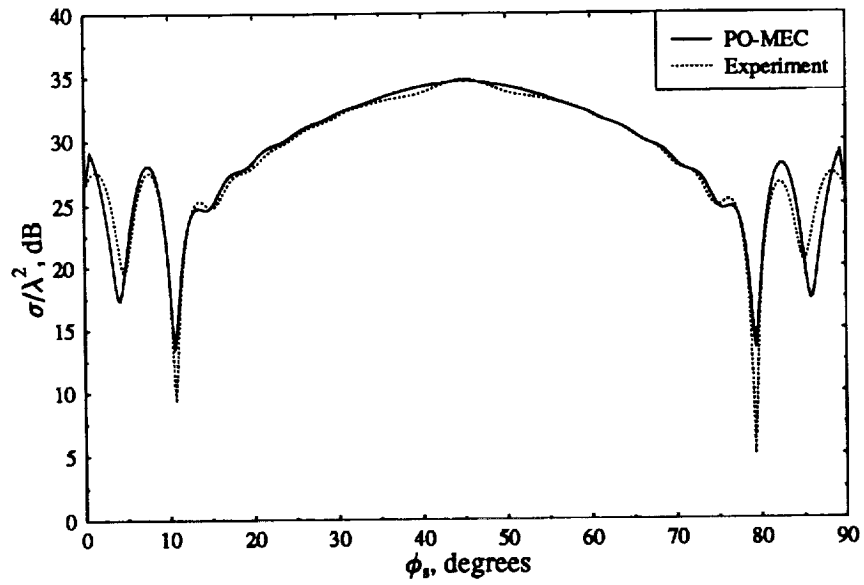


Figure 23: Monostatic RCS of a 7λ triangular trihedral on a great circle at $\theta_g = 80^\circ$.

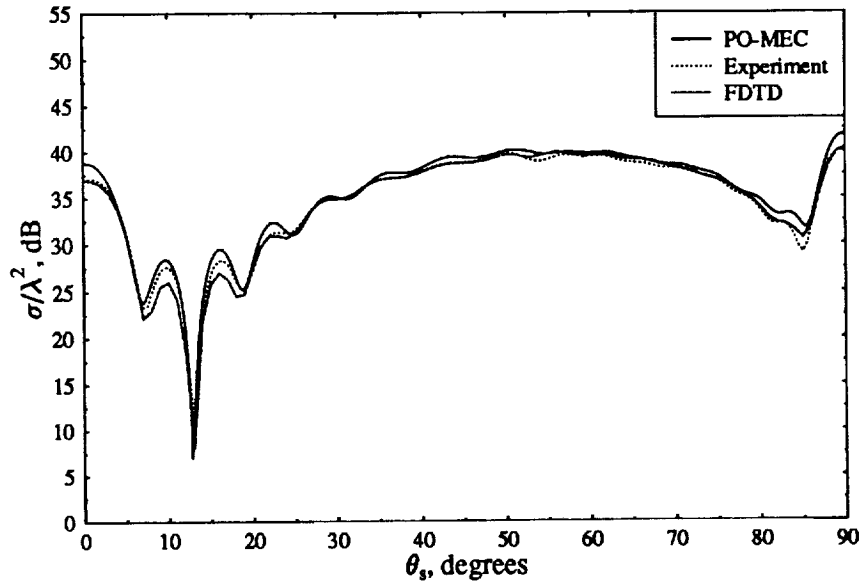


Figure 24: Monostatic RCS of a 7λ triangular trihedral at $\phi_i = \phi_s = 45^\circ$.

$\phi = 45^\circ$. This is always the case since the trihedral exhibits symmetry when the observation point moves on an azimuthal plane. Fig. 24 illustrates the monostatic RCS of a 7λ triangular trihedral at $\phi_i = \phi_s = 45^\circ$ as $\theta_i = \theta_s$ varies from 0° to 90° . Our predictions match very well with both the FDTD and the experiment.

3. Large Trihedral Corner Reflectors

A 7λ square trihedral and a 10λ triangular trihedral are considered relatively large radar targets. Fig. 25 shows the monostatic RCS of a 7λ square trihedral on a conical path as $\theta_i = \theta_s = 70^\circ$ and $\phi_i = \phi_s$ varies from 0° to 90° . The agreement of the PO-MEC with the experiment is very good. Fig. 26 shows the monostatic RCS of a 7λ square trihedral at $\phi_i = \phi_s = 50^\circ$ as $\theta_i = \theta_s$ varies from 0° to 90° . Our predictions agree very well with the FDTD data. Fig. 27 shows the monostatic RCS of a 10λ triangular trihedral as ϕ_s varies on a great circle at $\theta_s = 80^\circ$. The agreement of the PO-MEC with the experiment is very good except near $\phi_s = 7^\circ$;

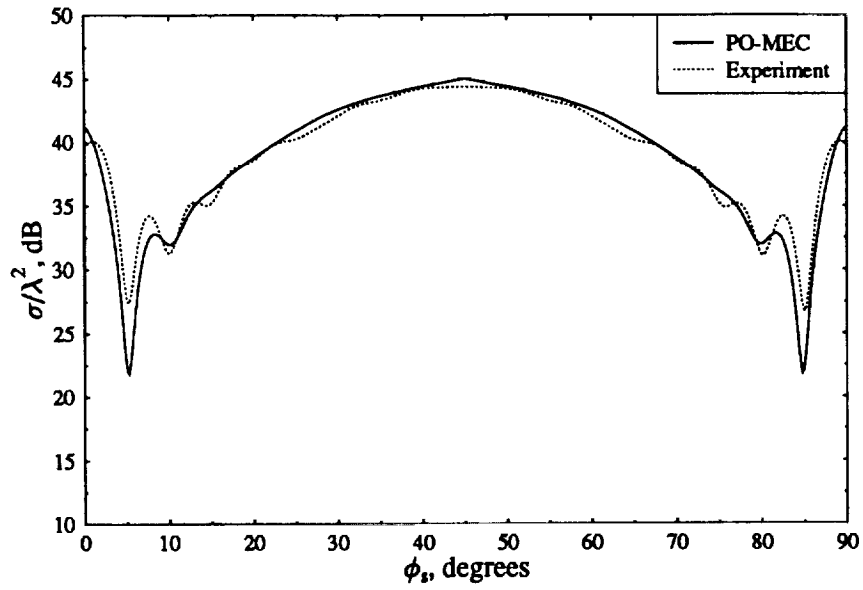


Figure 25: Monostatic RCS of a 7λ square trihedral at $\theta_i = \theta_s = 80^\circ$.

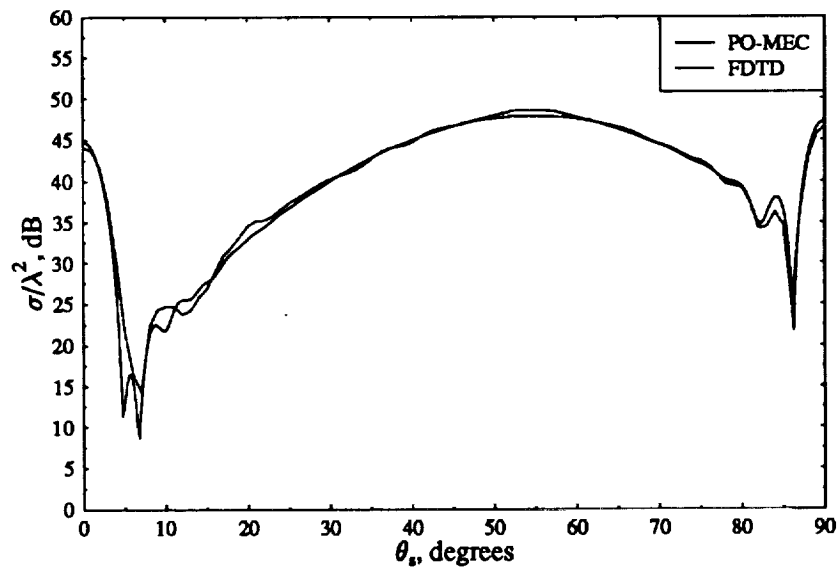


Figure 26: Monostatic RCS of a 7λ square trihedral at $\phi_i = \phi_s = 50^\circ$.

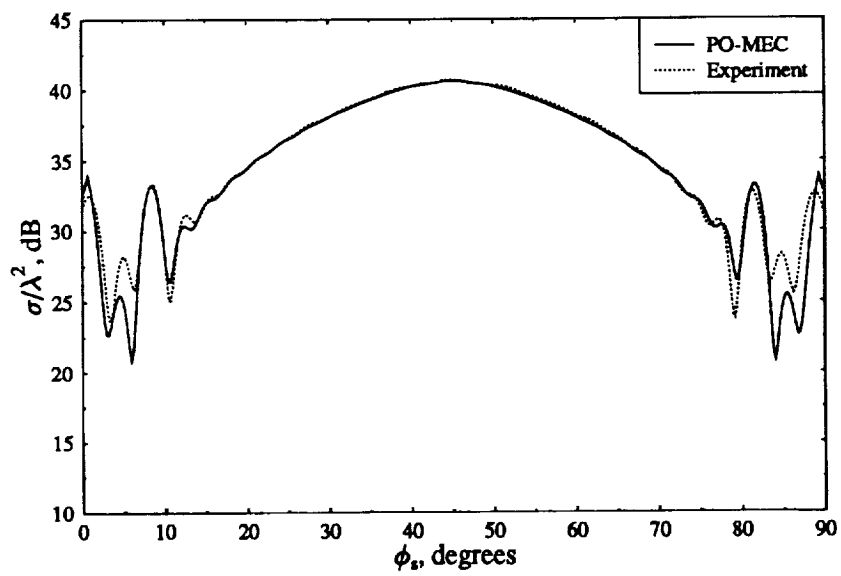


Figure 27: Monostatic RCS of a 10λ triangular trihedral on a great circle at $\theta_g = 80^\circ$.

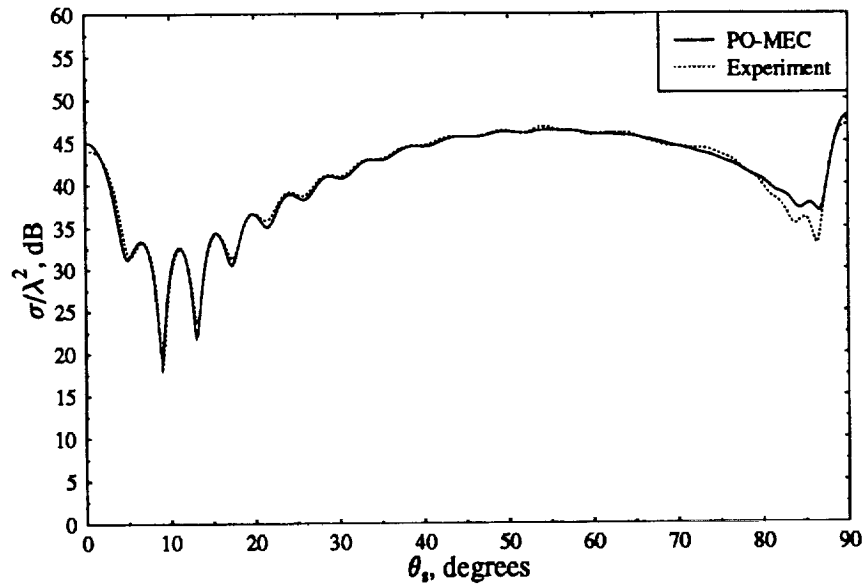


Figure 28: Monostatic RCS of a 10λ square trihedral at $\phi_i = \phi_s = 45^\circ$.

however, it was observed that near this specific observation angle the RCS pattern is very sensitive to slight changes in θ_g . Also, it can be seen from Fig. 27 that the experimental data is not quite symmetric about $\phi_s = 45^\circ$. Finally, Fig. 28 shows the monostatic RCS of a 10λ triangular trihedral at $\phi_i = \phi_s = 45^\circ$ as $\theta_i = \theta_s$ varies from 0° to 90° . Our predictions are in nearly excellent agreement with the experimental data.

The FORTRAN code written for the evaluation of the RCS of either the square or the triangular trihedral corner reflector provides very good results for any angle of incidence and/or observation. The agreement with experimental data is within 2 dB of accuracy. Fig. 29 and Fig. 30 show three-dimensional RCS patterns of a 5λ square trihedral and a 7λ triangular trihedral, respectively. The execution time required by a SUN SPARC station IPX computer to calculate the data to create either one of these three-dimensional plots is 77.4 seconds, which is much less than the execution time required by other theoretical techniques to

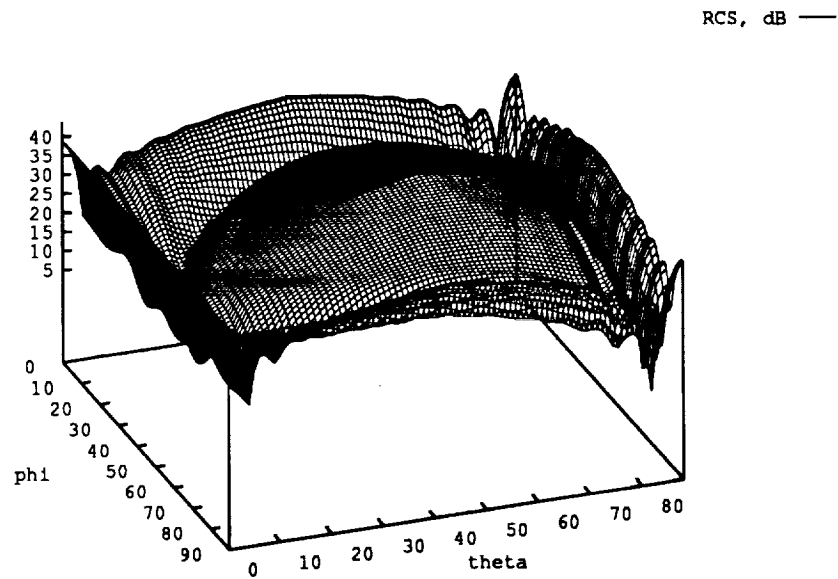


Figure 29: Three-dimensional monostatic RCS of a 5λ square trihedral.

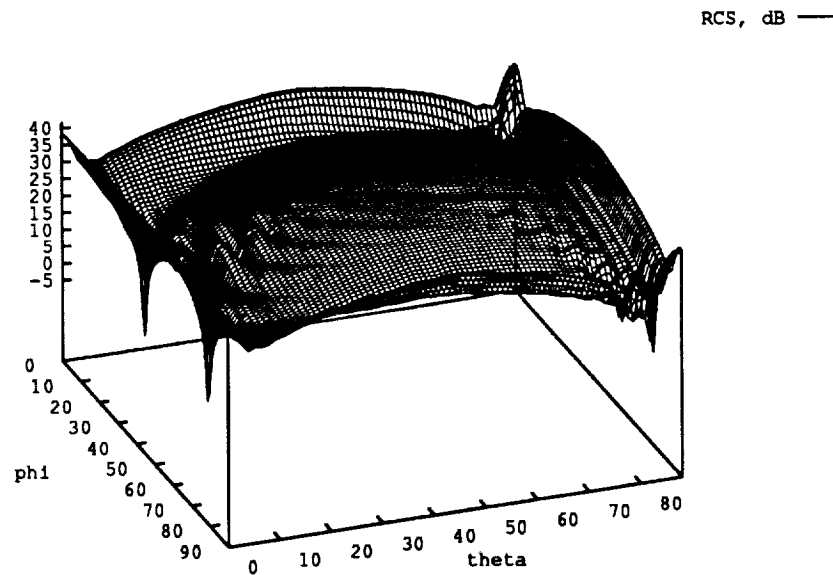


Figure 30: Three-dimensional monostatic RCS of a 7λ triangular trihedral.

perform the same task.

D. CONCLUSIONS

The hybridization of PO and MEC is a very good approach for the evaluation of the monostatic RCS of complex structures such as the square and triangular corner reflectors. It provides results that compare very well with experimental, as well as with FDTD data. The method is also very efficient in terms of computational requirements such as memory space and CPU time. For example, the FORTRAN code, which was used to obtain the results presented in this report, can compile and run on a variety of computer systems including a PC. It also runs very quickly. Specifically, it takes only 0.0095 seconds on a SUN SPARC station IPX computer to evaluate the RCS of either trihedral corner reflector at a single point. This CPU time is constant, regardless of the trihedral size.

E. FUTURE WORK

In this semiannual report we examined the monostatic RCS of both square and triangular trihedral corner reflectors in the interior region. In the future, we are planning to obtain the RCS of both these trihedrals in the exterior region as well. This will complicate the approach used to determine the illuminated area on the plate of last reflection.

References

- [1] C. A. Balanis and L. A. Polka, "Nonprincipal plane scattering of flat plates," Semiannual Report, Grant No. NAG-1-562, National Aeronautics and Space Administration, Langley Research Center, Hampton, VA, Jan. 31, 1989.
- [2] C. A. Balanis and L. A. Polka, "Nonprincipal plane scattering of flat plates — second-order and corner diffraction," Semiannual Report, Grant No. NAG-1-562, National Aeronautics and Space Administration, Langley Research Center, Hampton, VA, Jul. 31, 1989.
- [3] C. A. Balanis, L. A. Polka, and K. Liu, "Nonprincipal plane scattering from rectangular plates and pattern control of horn antennas," Semiannual Report,

Grant No. NAG-1-562, National Aeronautics and Space Administration, Langley Research Center, Hampton, VA, Jan. 31, 1990.

- [4] C. A. Balanis, L. A. Polka, and K. Liu, "Scattering from coated structures and antenna pattern control using impedance surfaces," Semiannual Report, Grant No. NAG-1-562, National Aeronautics and Space Administration, Langley Research Center, Hampton, VA, Jul. 31, 1990.
- [5] C. A. Balanis and L. A. Polka, "High-frequency techniques for RCS prediction of plate geometries," Semiannual Report, Grant No. NAG-1-562, National Aeronautics and Space Administration, Langley Research Center, Hampton, VA, Jan. 31, 1991.
- [6] C. A. Balanis and L. A. Polka, "High-frequency techniques for RCS prediction of plate geometries," Semiannual Report, Grant No. NAG-1-562, National Aeronautics and Space Administration, Langley Research Center, Hampton, VA, Jul. 31, 1991.
- [7] C. A. Balanis and L. A. Polka, "High-frequency techniques for RCS prediction of plate geometries," Semiannual Report, Grant No. NAG-1-562, National Aeronautics and Space Administration, Langley Research Center, Hampton, VA, Jan. 31, 1992.
- [8] C. A. Balanis and L. A. Polka, "High-frequency techniques for RCS prediction of plate geometries," Semiannual Report, Grant No. NAG-1-562, National Aeronautics and Space Administration, Langley Research Center, Hampton, VA, Jul. 31, 1992.
- [9] C. A. Balanis, L. A. Polka, and A. C. Polycarpou, "High-frequency techniques for RCS prediction of plate geometries and a physical optics/equivalent currents model for the RCS of trihedral corner reflectors," Semiannual Report, Grant No. NAG-1-562, National Aeronautics and Space Administration, Langley Research Center, Hampton, VA, Jan. 31, 1993.
- [10] C. M. Knop and G. I. Cohn, "On the radar cross section of a coated plate," *IEEE Trans. Antennas Propagat.*, vol. AP-11, pp. 719-721, Nov. 1963.
- [11] A. K. Bhattacharyya and S. K. Tandon, "Radar cross section of a finite planar structure coated with a lossy dielectric," *IEEE Trans. Antennas Propagat.*, vol. AP-32, pp. 1003-1007, Sept. 1984.
- [12] E. H. Newman and M. R. Schrote, "An open surface integral formulation for electromagnetic scattering by material plates," *IEEE Trans. Antennas Propagat.*, vol. AP-32, pp. 672-678, Jul. 1984.

- [13] R. Tiberio, G. Pelosi, and G. Manara, "A uniform GTD formulation for the diffraction by a wedge with impedance faces," *IEEE Trans. Antennas Propagat.*, vol. AP-33, pp. 867 – 873, Aug. 1985.
- [14] T. Griesser and C. A. Balanis, "Reflections, diffractions, and surface waves for an interior impedance wedge of arbitrary angle," *IEEE Trans. Antennas Propagat.*, vol. AP-37, pp. 927 – 935, Jul. 1989.
- [15] M. I. Herman and J. L. Volakis, "High frequency scattering from polygonal impedance cylinders and strips," *IEEE Trans. Antennas Propagat.*, vol. AP-36, pp. 679–689, May 1988.
- [16] J. L. Volakis and T. B. A. Senior, "Application of a class of generalized boundary conditions to scattering by a metal-backed dielectric half-plane," *Proc. IEEE*, vol. 77, pp. 796–805, May 1989.
- [17] R. G. Rojas and L. M. Chou, "Diffraction by a partially coated perfect electric conducting half plane," *Radio Sci.*, vol. 25, pp. 175–188, Mar. - Apr. 1990.
- [18] J.-M. L. Bernard, "Diffraction by a metallic wedge covered with a dielectric material," *Wave Motion*, vol. 9, pp. 543–561, Nov. 1987.
- [19] R. A. Ross, "Radar cross section of rectangular flat plates as function of aspect angle," *IEEE Trans. Antennas Propagat.*, vol. AP-14, pp. 329 – 335, May 1966.
- [20] G. D. Maliuzhinets, "Excitation, reflection and emission of surface waves from a wedge with given face impedances," *Sov. Phys. Doklady*, vol. 3, pp. 752 – 755, Jul./Aug. 1958.
- [21] T. B. A. Senior, *Derivation and Application of Approximate Boundary Conditions*, pp. 477–483. *Directions in Electromagnetic Wave Modeling (H. L. Bertoni and L. B. Felsen, eds.)*, New York: McGraw-Hill, 1969.
- [22] J. Baldauf, S. W. Lee, L. Lin, S. K. Jeng, S. M. Scarborough, and C. L. Yu, "High frequency scattering from trihedral corner reflectors and other benchmark targets: SBR versus experiment," *IEEE Trans. Antennas Propagat.*, vol. AP-39, pp. 1345–1351, Sep. 1991.
- [23] A. Michaeli, "Equivalent edge currents of arbitrary aspects of observation," *IEEE Trans. Antennas Propagat.*, vol. AP-32, pp. 252–258, Mar. 1984.
- [24] A. Michaeli, "Elimination of infinities in equivalent edge currents, part I: Fringe currents," *IEEE Trans. Antennas Propagat.*, vol. AP-34, pp. 912–918, Jul. 1986.
- [25] C. A. Balanis, *Advanced Engineering Electromagnetics*. New York: John Wiley and Sons, 1989.